CERN-INTC-2022-010 / INTC-P-625
12/01/2022

EUROPEAN ORGANIZATION FOR NUCLEAR RESEARCH

Proposal to the ISOLDE and Neutron Time-of-Flight Committee

Transfer reactions on the neutron-rich krypton isotopes

January 5, 2022

L. P. Gaffney[1], S. A. Bennett[2], F. Browne[3], P. A. Butler[1], A. Ceulemans[4], D. Clarke[2], A. Dolan[1], F. Flavigny[5], S. J. Freeman[3], K. Garrett[2], D. T. Joss[1], B. Kay[6], M. Labiche[7], I. Lazarus[7], P. T. MacGregor[2], J. Ojala[8], B. Olaizola[3], R. D. Page[1], O. Poleshchuk[4], R. Raabe[4], M.-M. Satrazani[1], D. K. Sharp[2], K. Wimmer[9]

[1] *University of Liverpool, UK*
[2] *The University of Manchester, UK*
[4] *KU Leuven, Belgium*
[5] *LPC Caen, France*
[3] *CERN-ISOLDE, Switzerland*
[6] *Argonne National Laboratory, USA*
[7] *STFC Daresbury Laboratory, UK*
[8] *University of Jyvaskyla, Finland*
[9] *GSI Helmholtzzentrum für Schwerionenforschung GmbH, Germany*

Spokespersons: L. P. Gaffney [liam.gaffney@liverpool.ac.uk]
Contact person: B. Olaizola [bruno.olaizola@cern.ch]

Abstract: We propose to investigate the onset of deformation in the neutron-rich krypton isotopes by studying the evolution of single-neutron properties towards $N = 60$. One-neutron transfer reactions, namely ^{92,94}Kr(d, p), will be performed in inverse kinematics using the ISOLDE Solenoidal Spectrometer at an energy of 7.5 MeV/u. Of particular interest in this study is the $\nu g_{7/2}$ orbital, which is filled in the ground states of krypton isotopes starting around $N = 59$ and is thought to lower the energy of the $\pi g_{9/2}$ orbital and help to drive deformation in this region. Information extracted from these data will be single particle energy differences and spectroscopic factors, allowing for comparison to modern shell-model calculations that try to describe the onset of deformation around $A = 100$.

Requested shifts: 23 shifts (split into 1 runs over 1 years)
Installations: ISS with Si array and gas ionisation chamber

1 Physics Case

The onset of deformation at $N = 60$***:*** The dramatic shape change observed in the $A = 100$ region for the zirconium ($Z = 40$) [1–5] and strontium ($Z = 38$) [6–12] isotopes is not observed in the krypton ($Z = 36$) isotopes, where there is a smooth reduction in 2_1^+ energies [13–15]. Correspondingly, the $B(E2; 2_1^+ \to 0_1^+)$ values also vary smoothly along the Kr isotopic chain, while both Sr and Zr display a large jump at $N = 60$ indicating a significant increase in ground state deformation. These systematic behaviours are shown in Figure 1 for the various isotopic chains in this region. Similar effects are also observed in two-neutron separation energy systematics from mass measurements [16].

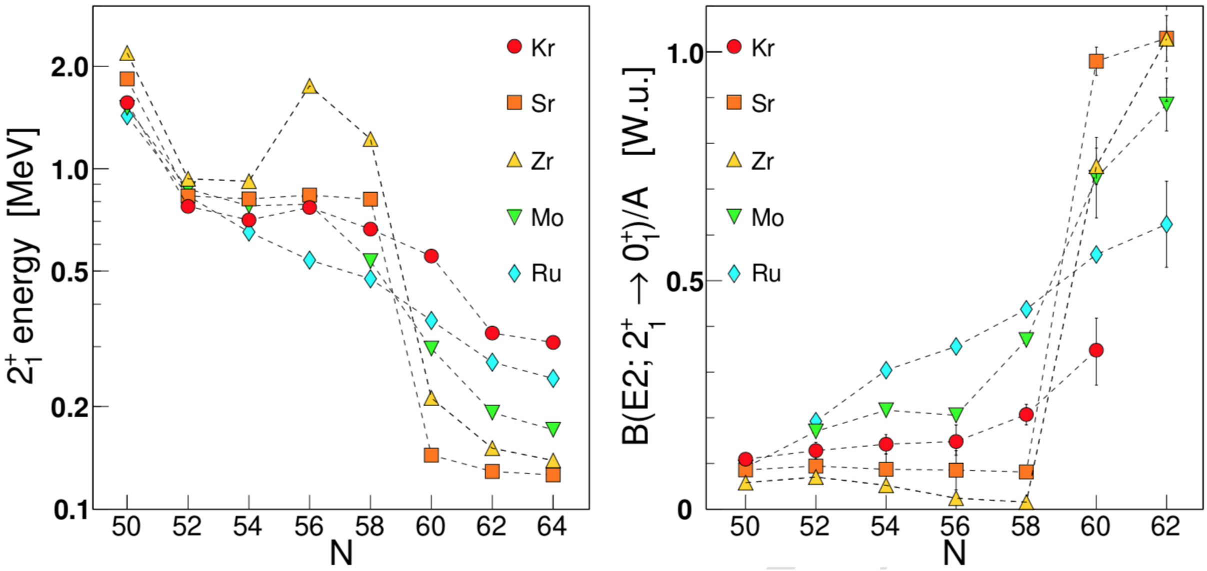

Figure 1: Systematics for $E(2_1^+)$ and $B(E2)$ values across $N = 60$ for Kr (red circles), Sr (orange squares), Zr (yellow up triangles), Mo (green down triangles) and Ru (blue diamonds) isotopic chains. The plot is reproduced from Ref. [17].

Single-particle origin of deformed states: Proton excitations across the $Z = 40$ sub-shell closure into the $0\pi g_{9/2}$ orbital are expected to be the driver of the deformed states in this region. These excitations were initially explained by a large overlap with the $0\nu g_{7/2}$ orbital, which begins filling around $N = 59$ [18]. More modern shell-model calculations for the Zr isotopes using a larger valence space confirm the role of the $0\pi g_{9/2}$ – $0\nu g_{7/2}$ interaction in driving deformation at $N = 60$ [19]. Large-scale Monte-Carlo Shell-Model (MCSM) calculations [20] show a dramatic increase in the occupancy number of the $0\pi g_{9/2}$ orbital from 0.4 to 3.5 between the spherical and prolate configurations in ^{98}Zr. The attractive neutron-proton interaction lowers the binding energy of this proton orbital as the $0\nu g_{7/2}$ orbital is filled, leading to a decrease in the effective single-particle energy (EPSE) difference to the $2\nu s_{1/2}$ orbital. The correlation between these two effects has been termed Type-II shell evolution [21] and gives rise to shape coexistence [22]. Recent results concerning the neutron-deficient mercury isotopes obtained with the MCSM indicate the importance of the attractive proton-neutron interaction in the description of one of the most striking examples of shape coexistence across the nuclear chart, this time between the $0\pi h_{9/2} - 0\nu i_{13/2}$ orbitals [23, 24]. A recent comprehensive review covering these topics can be found in Ref. [17].

Previous studies in this region: Shape coexistence in the neutron-rich Kr isotopes has been studied at REX-ISOLDE by means of Coulomb excitation of the even-even ^{92,94,96}Kr [14, 15]. The smooth onset of deformation at $N = 60$ is in contrast to the observations in the Sr isotopes in a similar study [9, 25], which is explained as a difference in the mixing between the two configurations in the different isotopic chains. More recently, spectroscopy of excited states has been extended to ^{98,100}Kr at the RIBF [26] showing the shape transition is complete and stabilises beyond $N = 60$. In addition, there is evidence of a new oblate structure coexisting with the prolate ground state, supported by mean-field calculations [27]. What is particularly interesting about these symmetry-conserving configuration-mixing results, consistent with a number of other calculations in this region, is the strong mixing observed in the competing configurations in $^{88-92}$Kr leading to near spherical shapes, which then gives way to deformed ground-states in $^{94-100}$Kr. While the observed shape transition at $N = 60$ in Sr, Zr, and Mo is reproduced in state-of-the-art beyond-mean-field calculations [8], accurately predicting ground-state spins and parities of odd-mass isotopes in this region is challenging. A more complete experimental picture of the low-energy structure of odd-mass isotopes in the region, in particular of the underlying single-particle configurations, is crucial to understand deformation around $A = 100$.

This proposal: We aim to study the evolution of the neutron occupancies and single-particle energy differences in the krypton isotopes near to $N = 60$ by means of one-neutron transfer. The main goals are to determine the energy difference between the $2\nu s_{1/2}$ and $0\nu g_{7/2}$ orbitals below $N = 60$ using the ^{92,94}Kr(d,p) reactions to identify the likely $\ell = 4$ transfer to the $7/2^+$ state. In ^{93}Kr, this state has been identified in a previous β-decay experiment at 354.7 keV [28] with the spin and parity assigned from systematics. Experiments at the RIBF during the SEASTAR campaign have only been able to build a limited level scheme in ^{95}Kr [29], but could confirm the previous identification of the isomeric state at 195.5 keV [30], which is proposed to be the $7/2^+$ state ($T_{1/2} = 1.582(22)$ μs).
Spectroscopic factors can be extracted by comparison of the measured cross-sections to DWBA calculations, which can be used to test shell-model calculations and infer the structure of the observed states. Fragmentation of both the $\ell = 0$ and $\ell = 4$ strength is expected due to the coupling to deformed core states. The $7/2^+$ state in the isotone ^{95}Sr was not directly observed in the previous ^{94}Sr(d,p) experiment at TRIUMF due to the low cross section combined with the isomeric nature of the state and the reliance on γ-ray detection [12]. By using the ISOLDE Solenoidal Spectrometer to analyse the proton ejectile directly, the latter problem is easily overcome. Additionally, the higher beam energy available at HIE-ISOLDE, up to 7.5 MeV/u versus 5.5 MeV/u at ISAC-II, should improve the sensitivity to the low cross sections.

2 Experiments

2.1 Beam production and yields

The radioactive beams of interest for this proposal are ^{92}Kr, ^{94}Kr and ^{96}Kr. Neutron-rich krypton beams have been produced a number of times at ISOLDE, including at REX-ISOLDE for Coulomb-excitation measurements at Miniball [15]. The production was from a UC_x target coupled to a VADIS ion-source [31], which ensures clean beams of noble gas elements. In the ^{96}Kr experiment of 2018, there was a very large contamination from stable ^{96}Mo, which is a component of a collimator in the new ion source. In previous experiments, a graphite-based ion source was used and this contamination was much reduced. Additionally, very weak contamination of the ^{94}Kr beam was observed from $^{188}Hg^{2+}$ ions from the primary target. Because of the very different mass and reaction kinematics, plus the release-time profile with respect to the proton impact time, this was not an issue for the Miniball experiment and can be easily separated using the ISS gas ionisation chamber should it be observed again.
Previously measured yields at Miniball are given in Table 1 along with those estimated using the yield database values, accounting for a 1.5 μA proton beam current, 5% charge breeding efficiency and 70% transmission through the linac. Due to the challenges posed

Table 1: Tabulated primary yields for the krypton isotopes from the ISOLDE yield database, along with the expected and previously measured yields [15] at the experimental station after post-acceleration. Also listed are the isotope half lives, which are important when considering beam contamination and losses from in-trap decay.

Isotope	$T_{1/2}$	Primary yield	Yield at ISS	Meas. yield at Miniball
^{92}Kr	1.84 s	1.0×10^8 ions/μC	5.2×10^6 pps	1.2×10^7 pps
^{94}Kr	212 ms	3.3×10^6 ions/μC	1.7×10^5 pps	4×10^5 pps
^{96}Kr	80 ms	1.3×10^5 ions/μC	6.8×10^3 pps	6×10^3 pps

by the short lifetime of ^{96}Kr, the yield at the experiment is strongly dependent on the trapping times required to achieve the required charge state in REX-EBIS [32]. With the upgrade of the EBIS gun during LS2 [33, 34] trapping times can be reduced in the future, improving this efficiency. However, this remains to be tested and no proposal will be made at the moment to study ^{96}Kr partly because of these limitations, as well as the unknown level density in ^{97}Kr and expected spectroscopic factors. Instead we are **requesting 1 shift** during the ^{92,94}Kr experiments to optimise the trapping time as well as test synchronisation between the PS-Booster proton impact and the REX-TRAP and REX-EBIS setup. Complementary measurements may provide input on the expected level density, while the proposed measurements here will inform on the spectroscopic factors and fragmentation of strength for a future proposal.

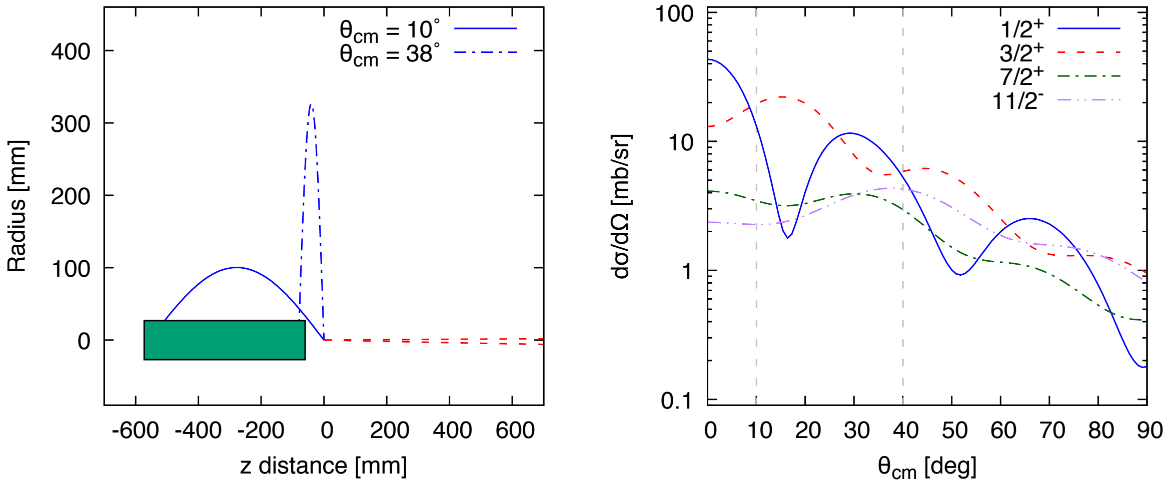

Figure 2: (Left) Kinematics for ^{92}Kr(d,p) in inverse kinematics at 7.5 MeV$/u$ using the ISOLDE Solenoidal Spectrometer with a magnetic field strength of 2.05 T. (Right) Cross-sections for $\ell = 0$, 2, 4 and 5 transfer to the $2\nu s_{1/2}$, $2\nu d_{3/2}$, $0\nu g_{7/2}$ and $0\nu h_{11/2}$ orbitals, respectively, using Ptolemy [35, 36], as described in the text. The vertical dashed lines mark the region covered by the on-axis array.

2.2 Transfer reactions at ISS

The new Liverpool-built on-axis silicon array will be used at ISS, positioned at a distance of 60 mm from the target in the upstream direction. The ISS magnet will be energised to 2.05 T, yielding an angular coverage in the centre-of-mass frame between 10° and 38° for the outgoing proton ejectiles in the ^{92,94}Kr(d,p) reactions. These kinematics are shown in the left-hand side of Figure 2. The gas ionisation chamber will be used, at a distance of 1.5 m from the target position, to identify coincidences with recoils on an event-by-event basis, giving a timing reference to clean up events in the on-axis silicon array. Recoils events can be further separated using the ΔE-E technique, eliminating fusion-evaporation events and giving some sensitivity to isobaric contamination and different reaction channels.

Cross sections are calculated with Ptolemy [35, 36] using global optical-model parameters, from Ref. [37] for protons and Ref. [38] for deuterons, and can be seen in Table 2. The beam energy is chosen as 7.5 MeV$/u$, corresponding to the maximum expected for HIE-ISOLDE, in order to maximise both the cross-section and sensitivity to the angular distributions. The reaction rates allow for states populated with spectroscopic factors down to $C^2S \approx 0.1$ to be probed. A silicon monitor detector will be placed $\approx$ 9 cm downstream from the target position to measure the elastic scattering of deuterons at $\approx 15°$, which can be used to obtain an absolute normalisation of the cross sections so that spectroscopic factors can be extracted from the data.

Simulations of the excitation energy spectra can be seen in Figure 3. The states of interest at low-energy can be easily resolved in ^{93}Kr with the expected resolution of 125 keV FWHM, while ^{95}Kr requires a more complex fitting. In order to extract the contributions of two different states in an unresolved doublet, i.e. the $3/2^+$ and $7/2^+$ states in ^{95}Kr, the

Table 2: Tabulated reaction cross sections for a number of states populated in the ^{92,94}Kr$(d,p)^{93,95}$Kr reactions, integrated over the angular coverage of the on-axis silicon array ($10° - 38°$). Also shown are count rates expected per 8-hour shift, assuming $C^2S = 0.1$, calculated yields from Table 1, a 100 μg/cm^2 target and a geometrical efficiency of $\epsilon_{\text{tot}} = \epsilon_\theta \cdot \epsilon_\phi = 94\% \cdot 70\% = 66\%$. We have assumed a rate limit in the ionisation chamber corresponding to a maximum of 1.0×10^6 pps on the ISS target.

	Energy	I^π	σ_{DWBA}	Counts per shift ($C^2S = 0.1$)
^{92}Kr$(d,p)^{93}$Kr	0 keV	$(1/2^+)$	10.4 mb	124
	117 keV	$(3/2^+)$	15.5 mb	184
	355 keV	$(7/2^+)$	4.6 mb	54
	–	$(11/2^-)$	4.4 mb	52
^{94}Kr$(d,p)^{95}$Kr	0 keV	$(1/2^+)$	10.1 mb	21
	114 keV	$(3/2^+)$	16.0 mb	33
	197 keV	$(7/2^+)$	4.8 mb	10
	–	$(11/2^-)$	5.1 mb	10

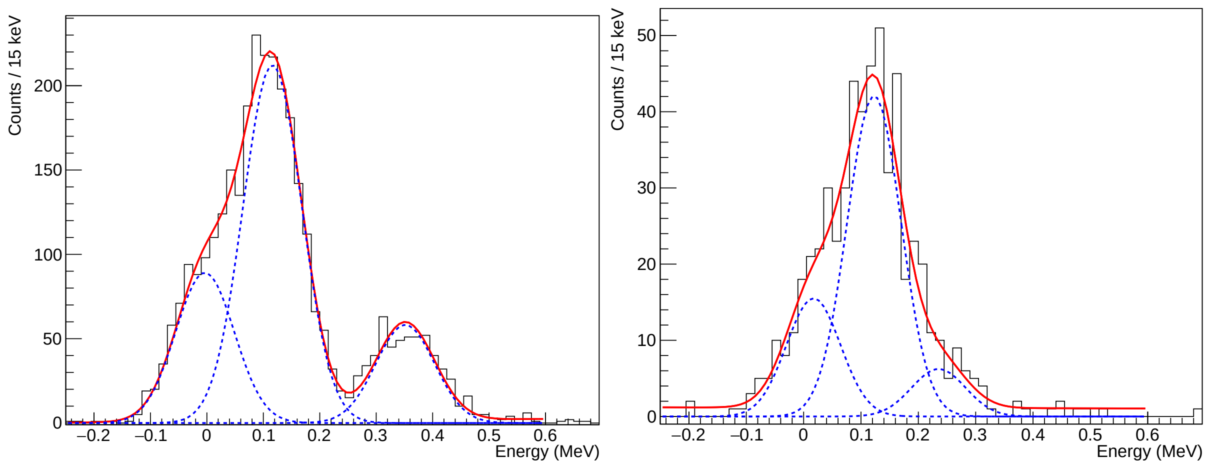

Figure 3: Simulated excitation energy spectra using NPTool for the ^{92}Kr$(d,p)^{93}$Kr (left) and ^{94}Kr$(d,p)^{95}$Kr (right) reactions for the expected intensities given in Table 2, assuming $C^2S = 0.1$. Only the lowest-lying three states in ^{93,95}Kr have been shown in these simulations, corresponding to transfer to the $s_{1/2}$, $d_{3/2}$ and $g_{7/2}$ states; more states are expected to be present at higher energy. The red line shows a fit to the simulated data (black) assuming three Gaussian peaks with a common width and all other variables free. The component peaks of the fit are indicated by the dashed blue line, demonstrating that the peaks can be separated with an obtained FHWM of ≈ 125 keV.

full angular distributions can be fitted for both states as was done for the ground-state doublet in ^{29}Mg [39]. The intensities shown in Fig. 3 assumes $C^2S = 0.1$ for all states, which is not expected to be the case, but represents a lower expectations of what can be observed in this proposal.

3 Beam time request

In order to be able to extract spectroscopic factors for the states of interest down to $C^2S \geq 0.1$ and obtain a minimum of 500 counts across the array, **10 shifts** are required for the ^{92}Kr$(d,p)^{93}$Kr measurement. The high statistics obtained in this measurement will also give sensitivity to fragmentation of the cross-section to higher-lying states in ^{93}Kr. We aim for a minimum of only 100 counts across the array in the ^{94}Kr$(d,p)^{95}$Kr measurement due to the lower ^{94}Kr beam intensity, corresponding to a request of **10 shifts**. In addition we require **1 shift** for the mass change and subsequent retune of the linac, plus half a shift on each mass to optimise the delivery of the beam on to the ISS target (total of **1 shift**).

Summary of requested shifts: We are requesting a total of **23 shifts**: ^{92}Kr (10.5 shifts), ^{94}Kr (10.5 shifts), ^{96}Kr (1 shift), and mass change (1 shift).

References

[1] E. Cheifetz, R. C. Jared, S. G. Thompson, and J. B. Wilhelmy, Physical Review Letters **25**, 38 (1970).
[2] H. L. Thayer et al., Journal of Physics G: Nuclear and Particle Physics **29**, 2247 (2003).
[3] F. Browne et al., Physics Letters B **750**, 448 (2015).
[4] J. E. García-Ramos and K. Heyde, Physical Review C **100**, 044315 (2019).
[5] P. Spagnoletti et al., Physical Review C **100**, 014311 (2019).
[6] F. Buchinger et al., Physical Review C **41**, 2883 (1990).
[7] H. Mach et al., Nuclear Physics A **523**, 197 (1991).
[8] R. Rodríguez-Guzmán, P. Sarriguren, L. M. Robledo, and S. Perez-Martin, Physics Letters B **691**, 202 (2010).
[9] E. Clément et al., Physical Review Letters **116**, 022701 (2016).
[10] A. Chester et al., Physical Review C **96**, 011302 (2017).
[11] J. M. Régis et al., Physical Review C **95**, 1 (2017).
[12] S. Cruz et al., Physical Review C **100**, 054321 (2019).
[13] M. Keim et al., Nuclear Physics A **586**, 219 (1995).
[14] M. Albers et al., Physical Review Letters **108**, 062701 (2012).
[15] M. Albers et al., Nuclear Physics A **899**, 1 (2013).
[16] S. Naimi et al., Physical Review Letters **105**, 032502 (2010).
[17] P. E. Garrett, M. Zielińska, and E. Clément, Progress in Particle and Nuclear Physics **163**, 103931 (2021).
[18] P. Federman and S. Pittel, Physics Letters B **69**, 385 (1977).

[19] K. Sieja, F. Nowacki, K. Langanke, and G. Martínez-Pinedo, Physical Review C **79**, 064310 (2009).
[20] T. Togashi, Y. Tsunoda, T. Otsuka, and N. Shimizu, Physical Review Letters **117**, 172502 (2016).
[21] Y. Tsunoda, T. Otsuka, N. Shimizu, M. Honma, and Y. Utsuno, Physical Review C **89**, 031301 (2014).
[22] T. Otsuka and Y. Tsunoda, Journal of Physics G: Nuclear and Particle Physics **43**, 024009 (2016).
[23] B. A. Marsh et al., Nature Physics **14**, 1163 (2018).
[24] S. Sels et al., Physical Review C **99**, 044306 (2019).
[25] E. Clément et al., Physical Review C **94**, 054326 (2016).
[26] F. Flavigny et al., Physical Review Letters **118**, 242501 (2017).
[27] T. R. Rodríguez, Physical Review C - Nuclear Physics **90**, 034306 (2014).
[28] G. Lhersonneau, A. Wöhr, B. Pfeiffer, K.-L. Kratz, and the ISOLDE Collaboration, Physical Review C **63**, 034316 (2001).
[29] D. Kameda et al., Physical Review C **86**, 054319 (2012).
[30] J. Genevey et al., Physical Review C - Nuclear Physics **73**, 037308 (2006).
[31] L. Penescu, R. Catherall, J. Lettry, and T. Stora, Review of Scientific Instruments **81**, 02A906 (2010).
[32] F. Wenander, Journal of Instrumentation **5**, C10004 (2010).
[33] A. Pikin, H. Pahl, and F. Wenander, Physical Review Accelerators and Beams **23**, 103502 (2020).
[34] H. Pahl, N. Bidault, G. Khatri, A. Pikin, and F. J. C. Wenander, Physical Review Accelerators and Beams (Accepted) (2022).
[35] M. Macfarlane and S. Pieper, Argonne National Laboratory Reports **76**, 11 (1978).
[36] M. Rhoades-Brown, M. H. MacFarlane, and S. C. Pieper, Physical Review C **21**, 2436 (1980).
[37] A. Koning and J. Delaroche, Nuclear Physics A **713**, 231 (2003).
[38] H. An and C. Cai, Physical Review C **73**, 054605 (2006).
[39] P. T. MacGregor et al., Physical Review C **104**, L051301 (2021).

Appendix

DESCRIPTION OF THE PROPOSED EXPERIMENT

The experimental setup comprises: *The ISOLDE Solenoidal Spectrometer*

Part of the	Availability	Design and manufacturing
ISOLDE Solenoidal Spectrometer	☒ Existing	☒ To be used without any modification ☐ To be modified
	☐ New	☐ Standard equipment supplied by a manufacturer ☐ CERN/collaboration responsible for the design and/or manufacturing

HAZARDS GENERATED BY THE EXPERIMENT (if using fixed installation:) Hazards named in the document relevant for the fixed ISS installation.

Additional hazards:

Hazards	ISS		
Thermodynamic and fluidic			
Pressure			
Vacuum			
Temperature			
Heat transfer			
Thermal properties of materials			
Cryogenic fluid			
Electrical and electromagnetic			
Electricity			
Static electricity			
Magnetic field	2.5 T		
Batteries			
Capacitors			
Ionizing radiation			
Target material	Deuterated polyethylene, CD_2 (50-400 μg/cm^2)		
Beam particle type	^{96}Kr		
Beam intensity	1.0×10^6		
Beam energy	7.5 MeV/u		
Cooling liquids			
Gases			
Calibration sources:	☒		

• Open source	☒ (α calibrations source 4236RP)		
• Sealed source			
• Isotope	^{148}Gd, ^{239}Pu, ^{241}Am, ^{244}Cm		
• Activity	1 kBq, 1 kBq, 1 kBq, 1 kBq = 4 kBq		
Use of activated material:			
• Description			
• Dose rate on contact and in 10 cm distance			
• Isotope			
• Activity			
Non-ionizing radiation			
Laser			
UV light			
Microwaves (300MHz-30 GHz)			
Radiofrequency (1-300 MHz)			
Chemical			
Toxic			
Harmful			
CMR (carcinogens, mutagens and substances toxic to reproduction)			
Corrosive			
Irritant			
Flammable			
Oxidizing			
Explosiveness			
Asphyxiant			
Dangerous for the environment			
Mechanical			
Physical impact or mechanical energy (moving parts)			
Mechanical properties (Sharp, rough, slippery)			
Vibration			
Vehicles and Means of Transport			

Noise			
Frequency			
Intensity			
Physical			
Confined spaces			
High workplaces			
Access to high workplaces			
Obstructions in passageways			
Manual handling			
Poor ergonomics			

Hazard identification:

Average electrical power requirements (excluding fixed ISOLDE-installation mentioned above): N/A